Characterization of Bias of Advanced Himawari Imager Infrared Observations from NWP Background Simulations Using CRTM and RTTOV

X. ZOU

Earth System Science Interdisciplinary Center, University of Maryland, College Park, College Park, Maryland

X. ZHUGE

*Earth System Science Interdisciplinary Center, University of Maryland, College Park, College Park, Maryland,
and School of Atmospheric Sciences, and Key Laboratory of Mesoscale Severe Weather, Ministry
of Education, Nanjing University, Nanjing, China*

F. WENG

NOAA/NESDIS/Center for Satellite Applications and Research, College Park, Maryland

(Manuscript received 17 May 2016, in final form 9 August 2016)

ABSTRACT

Starting in 2014, the new generation of Japanese geostationary meteorological satellites carries an Advanced Himawari Imager (AHI) to provide the observations of visible, near infrared, and infrared with much improved spatial and temporal resolutions. For applications of the AHI measurements in numerical weather prediction (NWP) data assimilation systems, the biases of the AHI brightness temperatures at channels 7–16 from the model simulations are first characterized and evaluated using both the Community Radiative Transfer Model (CRTM) and the Radiative Transfer for the TIROS Operational Vertical Sounder (RTTOV). It is found that AHI biases under a clear-sky atmosphere are independent of satellite zenith angle except for channel 7. The biases of three water vapor channels increase with scene brightness temperatures and are nearly constant except at high brightness temperatures for the remaining infrared channels. The AHI biases at all the infrared channels are less than 0.6 and 1.2 K over ocean and land, respectively. The differences in biases between RTTOV and CRTM with the land surface emissivity model used in RTTOV are small except for the upper-tropospheric water vapor channels 8 and 9 and the low-tropospheric carbon dioxide channel 16. Since the inputs used for simulations are the same for CRTM and RTTOV, the differential biases at the water vapor channels may be associated with subtle differences in forward models.

1. Introduction

The Advanced Himawari Imager (AHI) on board the Japanese satellite *Himawari-8* (Bessho et al. 2016) is the first of the new generation of geostationary imagers among global meteorological observation systems. Similar instruments, the Advanced Geostationary Radiation Imager (AGRI), the Advanced Baseline Imager (ABI), and the Flexible Combined Imager (FCI) will be on board the Chinese satellite Fengyun–4A (Lu 2013), the U.S. Geostationary Operational Environmental Satellite (GOES)-R (Schmit et al. 2005, 2016), and the European Meteosat Third Generation (MTG)–Imaging 1 (MTG-I1; Ouaknine et al. 2013), respectively. The AHI/*Himawari-8* was launched by the Japanese Meteorological Agency on 7 October 2014. It is now positioned in geostationary orbit nominally at 140.7°E and is perched at 35 800 km above the equator. Compared to all earlier geostationary imagers, the AHI observes the earth's atmosphere with much higher spectral, temporal, and spatial resolutions.

The geostationary imager observations are critical for national weather services and nowcasting applications. The visible and infrared measurements from geostationary

ⓐ Denotes Open Access content.

Corresponding author address: Dr. Xiaolei Zou, Earth System Science Interdisciplinary Center, University of Maryland, College Park, 5825 University Research Court, Office 4078, College Park, MD 20740-3823.
E-mail: xzou1@umd.edu

TABLE 1. AHI channel characteristics of central wavelength, bandwidth, WF peak, spatial resolution at the satellite subpoint (SSP), SNR at 100% albedo for visible and near-infrared channels, and noise-equivalent differential temperature (NEdT) for infrared channels.

Channel No.		Central λ (μm)	Bandwidth (μm)	WF peak (hPa)	Spatial resolution at SSP (km)	SNR or NEdT
Visible	1	0.46	0.041	—	1	≥300 (100% albedo)
	2	0.51	0.031		1	
	3	0.65	0.081		0.5	
Near infrared	4	0.86	0.035		1	
	5	1.61	0.041		2	
	6	2.26	0.044			
Infrared	7	3.85	0.201	Surface		≤0.16 (300 K)
	8	6.25	0.822	377		≤0.40 (240 K)
	9	6.95	0.402	457		≤0.10 (300 K)
	10	7.35	0.187	587		≤0.32 (240 K)
	11	8.60	0.373	Surface		≤0.10 (300 K)
	12	9.63	0.378	40		
	13	10.45	0.419	Surface		
	14	11.20	0.668			
	15	12.35	0.966			
	16	13.30	0.564	996		≤0.30 (300 K)

imagers are used to retrieve cloud information, such as particle size and cloud-top properties (Mecikalski et al. 2008). The infrared and water vapor imageries are utilized to derive the atmospheric motion vectors by tracking the movements of clouds and water vapor fields (e.g., Velden 1996; Velden et al. 1997, 1998). The retrieved products are used for analyzing and defining the weather systems from their preconvective environments to occurrence and evolution (Mecikalski and Bedka 2006; Mecikalski et al. 2015; Gravelle et al. 2016). Recently, it was also demonstrated that geostationary imager radiance assimilation improves the forecast skill of fast-evolving weather systems (Stengel et al. 2009; Zou et al. 2011, 2015). The applications in atmospheric parameter retrievals and numerical weather prediction (NWP) demand an accurate calibration/validation (cal/val) of the geostationary imager data.

The AHI on board *Himawari-8* has 3 visible, 3 near-infrared, and 10 infrared channels. Yu and Wu (2016) evaluated the calibration accuracy of AHI visible and near-infrared channels 1–6 by comparing them with the

TABLE 2. Input variables and parameters for clear-sky simulations with CRTMv2.2.3.

Category	Variable name	Unit	Data resource
Atmosphere variables	Level and layer pressure	hPa	ECMWF analysis
	Temperature	K	
	Water vapor mixing ratio	ppmv	
	O_3 mixing ratio		
	CO_2 mixing ratio		Constant (376)
Surface variables	Land type	—	One-Minute Land Ecosystem Classification Product[a]
	Skin temperature	K	ECMWF analysis
	Water type	—	Always 1 (seawater)
	Wind speed	m s^{-1}	ECMWF analysis
	Wind direction	Degrees	
Geometry	Terrestrial elevation	m	Global 30 arc s elevation dataset[b]
	Satellite zenith angle	Degrees	Calculated according to longitude and latitude
	Satellite azimuth angle		
	Solar zenith angle		
	Solar azimuth angle		
Parameters	Climatology	—	U.S. standard profile
	Land coverage	—	1 for land and 0 for ocean
	Water coverage		0 for land and 1 for ocean
	Snow coverage		Always 0
	Ice coverage		Always 0
	Land surface classification scheme	—	IGBP

[a] http://modis-atmos.gsfc.nasa.gov/ECOSYSTEM/index.html; the "land type" is not needed by RTTOV.
[b] http://webmap.ornl.gov/ogcdown/dataset.jsp?ds_id=10003.

Visible Infrared Imaging Radiometer Suite (VIIRS) on board the *Suomi–National Polar-Orbiting Partnership* satellite. It was demonstrated that AHI reflectance quality agrees well with that of VIIRS data within 5% for channels 1–4 and 6, while AHI channel 5 is generally brighter than VIIRS by ~6%–8%. However, there are still no publications that present the convincing results of the val/cal of AHI infrared channels.

Applications of geostationary imager radiance data in NWP systems are limited to infrared channels (Köpken et al. 2004; Szyndel et al. 2005; Stengel et al. 2009; Zou et al. 2011; Qin et al. 2013; Zou et al. 2015). Before AHI infrared radiances can be assimilated into global and regional NWP systems, it is important to properly quantify the biases of the 10 AHI infrared channels. In this study, the AHI data biases are estimated by the differences between observations and simulations obtained by using two widely used radiative transfer models. The paper is organized as follows: Section 2 provides AHI data characteristics. The two fast radiative transfer models and input data for AHI simulations are briefly described in section 3. Biases and standard deviations estimated for AHI infrared channels 7–16 are presented and compared in section 4. The scene and satellite zenith angle dependences of AHI biases and the impacts of land surface emissivity on biases of AHI surface-sensitive channels are discussed. Summary and conclusions are provided in section 5.

2. AHI data characteristics

The AHI instrument on board *Himawari-8* is designed for 8 years of service for observing potentially life-threatening weather, including tropical storm activity in the Pacific Ocean at a full Earth imaging refresh rate of 10 min (Clark 2014). Table 1 presents the center wavelengths, bandwidths, spatial resolutions, and measurement precisions for AHI visible, near-infrared, and infrared channels. A consistent spatial resolution of 2 km for all AHI infrared channels is apparently beneficial for assimilating AHI multichannel radiance data and for deriving AHI multichannels products based on spectral differences, such as cloud mask algorithms (Heidinger 2011). Out of the 16 AHI channels, AHI channels 8–10 are strongly affected by water vapor in the middle and upper troposphere. AHI channel 12 is affected by stratospheric ozone, and channel 16 is affected by carbon dioxide in the low troposphere.

3. Radiative transfer models

The Community Radiative Transfer Model (CRTM) and the Radiative Transfer for the TIROS Operational Vertical Sounder (RTTOV) are two widely used fast
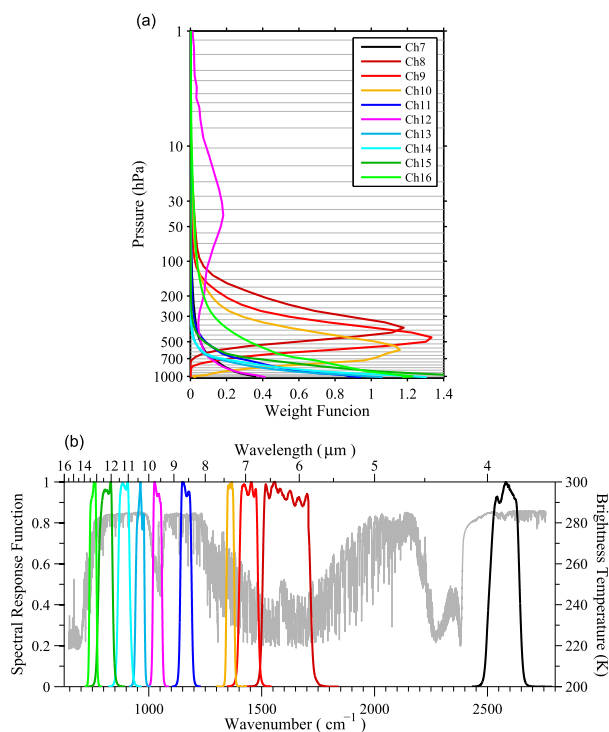

FIG. 1. (a) Weighting functions of AHI infrared channels calculated by using CRTM with a clear-sky atmosphere profile as the input. The ECMWF model levels are indicated by gray horizontal lines. (b) Spectral response functions of the AHI on board *Himawari-8*, accompanied with typical brightness temperatures simulated with CRTM and an IASI coefficient file (gray thin curve).

radiative transfer models. CRTM was developed by the U.S. Joint Center for Satellite Data Assimilation (JCSDA) (Weng 2007; Han et al. 2007). RTTOV was originally developed by Saunders et al. (1999) and is maintained by the European Centre for Medium-Range Weather Forecasts (ECMWF) (Matricardi et al. 2004). Both models support a large number of sensors on board historical and current geostationary/polar-orbiting satellites, including AHI on board *Himawari-8*. Specifically, model simulations of clear-sky radiances are generated by CRTM or RTTOV with any given vertical profiles of atmospheric temperature, water vapor and composition, surface temperature, and surface wind speed, as well as solar and sensor geometry parameters. For cloudy radiance simulation, which is not considered for this study, vertical profiles of hydrometeor variables (e.g., cloud liquid water path and ice water path) are also required.

A detailed description of input variables and parameters for clear-sky radiance simulations with CRTM, version 2.2.3 (CRTMv2.2.3), is provided in Table 2. The three-dimensional variables of temperature, water vapor, pressure, and ozone mixing ratio, as well as the two-dimensional variables of surface skin temperature,
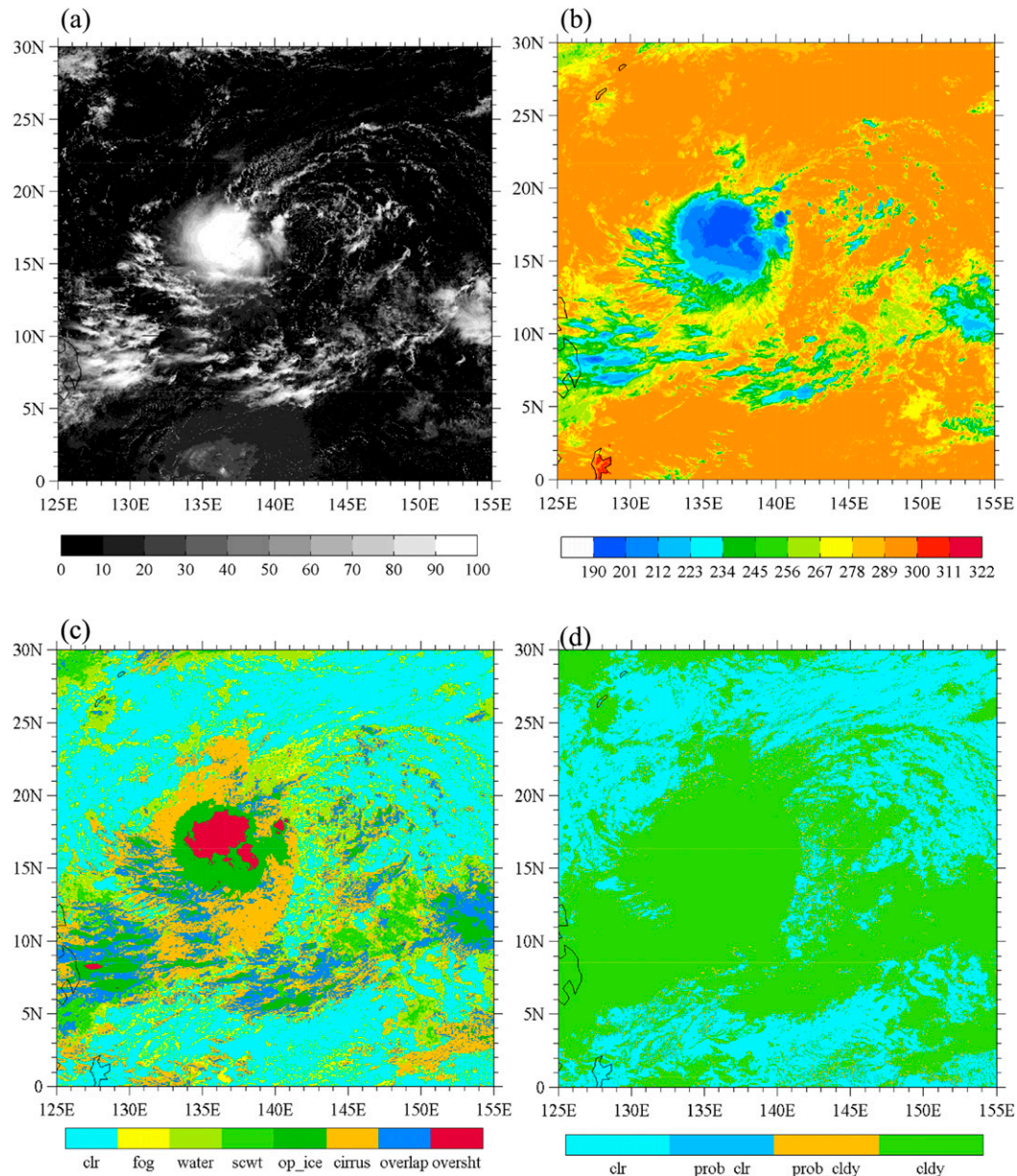
FIG. 2. (a) Albedo of AHI visible channel 3; (b) brightness temperatures of AHI channel 14; (c) AHI-derived cloud types, including clear (clr, cyan), fog (yellow), water (light green), supercooled water (scwt, green), opaque ice (op_ice, forest green), cirrus (orange), overlapping (overlap, blue), and overshooting (oversht, red); and (d) AHI-derived clear (clr), probably clear (prob_clr), probably cloudy (prob_cldy), and cloudy (cldy) pixels at 0300 UTC 22 Sep 2015.

surface wind speed, and surface wind direction, are obtained from ECMWF analyses, which are available at a 6-h interval. The ECMWF data have a horizontal resolution of $0.25° \times 0.25°$, 91 vertical levels, and a model top around 0.01 hPa. The mixing ratio profile of carbon dioxide is set to a constant value of 376 ppmv. The land type and terrestrial elevation required by CRTMv2.2.3 are extracted from the One-Minute Land Ecosystem Classification Product and the global 30 arc s elevation dataset, respectively. The input variables and parameters required by RTTOV, version 11.2 (RTTOVv11.2), for clear-sky radiance simulations are similar to CRTM except for the land type, which is not needed for RTTOV. In addition, as a shortwave infrared channel, AHI channel 7 could be impacted by the solar radiance contribution, especially in the presence of sea surface reflection.
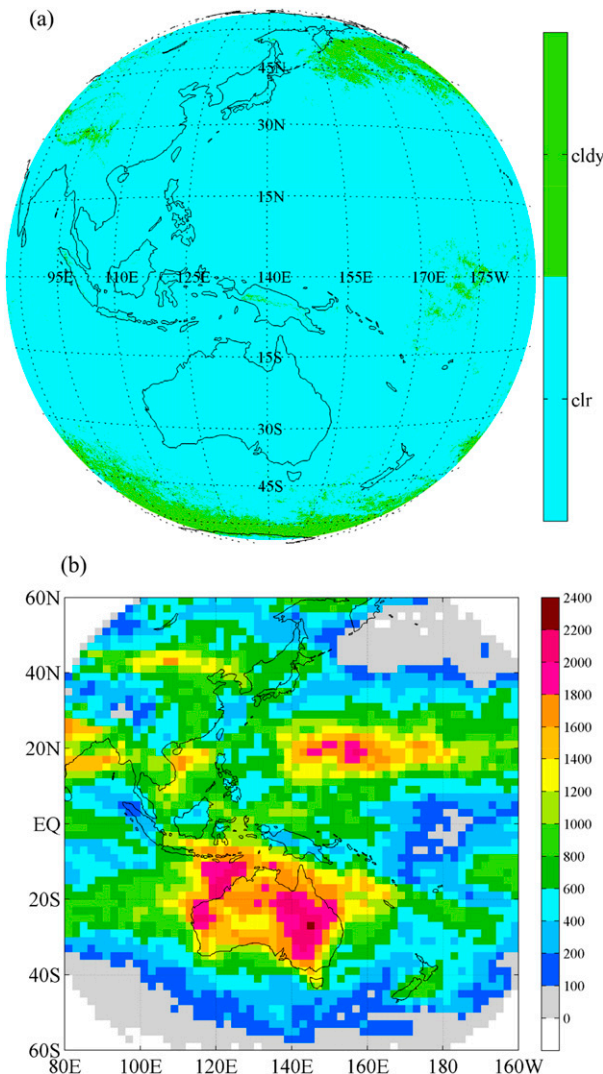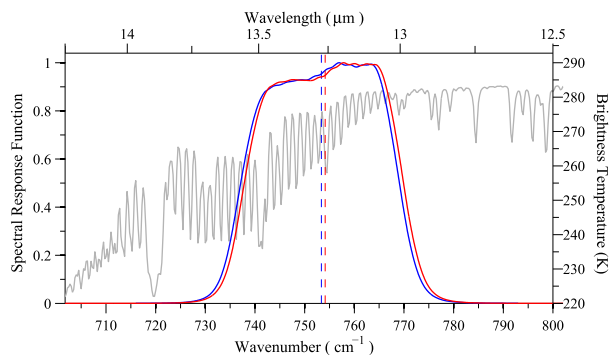
FIG. 4. Spectral response functions (curves) and the center frequencies of AHI channel 16 with (blue) and without (red) using the updated SRFs, as well as typical IASI brightness temperatures simulated with CRTM (gray).

us to select only those AHI data that are identified certainly as clear for AHI bias estimation. Data flagged probably clear, cloudy, or probably cloudy are excluded for the bias estimate of AHI data conducted in this study.

4. Numerical results

a. Vertical and spectral distributions of AHI infrared channels and clear-sky data distribution

Figure 1a shows the weighting functions (WFs) of the 10 AHI infrared channels calculated using CRTM with a clear-sky atmosphere profile as the input. The spectral response functions (SRFs) of the AHI on board *Himawari-8* are provided in Fig. 1b, in which a typical variation of brightness temperatures simulated with CRTM in the infrared part of the electromagnetic spectrum at all wavenumbers observed by the Infrared Atmospheric Sounding Interferometer (IASI) is included as reference. Most AHI infrared channels are surface channels with WF peaks located at the surface or near surface except for three water vapor channels. The water vapor channel 8 located in the upper troposphere is similar to imager channel 3 from *GOES-11*, *-12*, *-13*, and *-15*. The AHI channels 9 and 10, with their peak WFs located at 457 and 587 hPa, respectively, shall provide much needed water vapor information in the middle and low troposphere for capturing short-term environmental changes with respect to timing and location of the occurrence and evolution of new convective storms and severe weather signatures. The WF of AHI channel 12 has two peaks, one located at the surface and the other at 40 hPa, where ozone concentration is abundant. The AHI channel 16 is a carbon dioxide channel and is located along the spectral radiances (Fig. 1b) with a strong slope. Since carbon dioxide is well mixed in the atmosphere, this channel is in fact a low-tropospheric temperature-sounding channel.
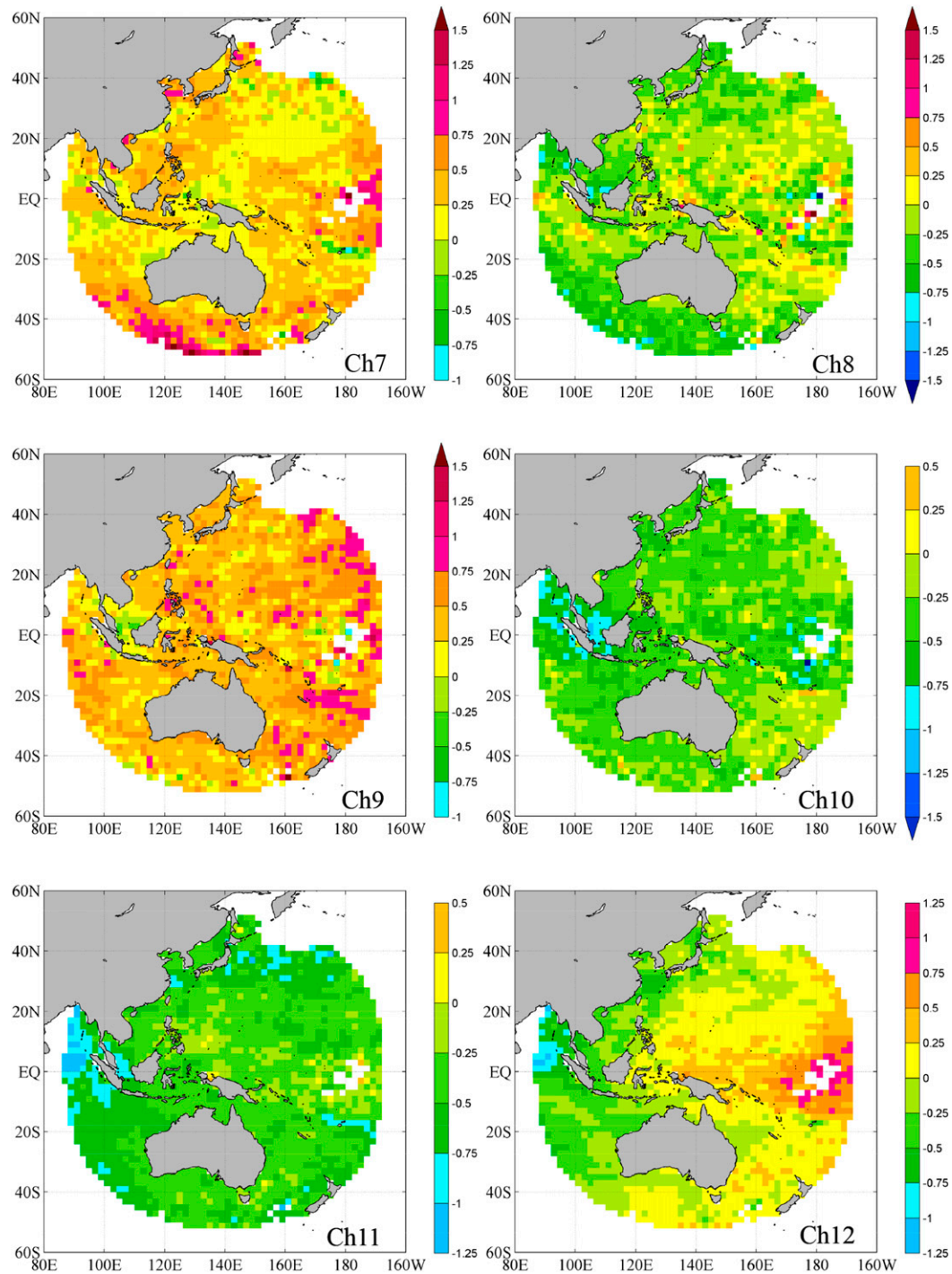

FIG. 3. (a) Composite map of areas that had clear pixels at least once (cyan) or no clear pixels (green), and (b) total data counts of clear-sky pixels within 2° × 2° grid boxes during 12 days: 22–24 Sep and 15–17 Dec 2015, as well as 20–22 Mar and 5–7 Jun 2016.

Such a solar reflection effect is taken into account in both the CRTM and RTTOV simulations.

Because the temporal and spatial resolutions of AHI observations and ECMWF analyses are different, only the data at the ECMWF analyses time and grid points were used. The cloud mask required by this study for determining clear-sky AHI data is obtained from the Clouds from Advanced Very High Resolution Radiometer (AVHRR) Extended (CLAVR-x) (Heidinger et al. 2012).[1] The ability for CLAVR-x to identify clear pixels from cloudy pixels with small uncertainties allows

---

[1] ftp://ftp.ssec.wisc.edu/clavr/.

FIG. 5. Spatial distributions of $O - B^{CRTM}$ biases of AHI channels 7–16 over ocean within $2° × 2°$ grid boxes.

The AHI brightness temperature measurements in clear-sky conditions required by the bias estimation are selected based on the CLAVR-x AHI cloud masks. A cloud mask example within and around Typhoon Dujuan at 0300 UTC 22 September 2015 is provided in Fig. 2. It is seen that clouds with high albedo (Fig. 2a) are spatially well correlated with the low brightness temperatures of channel 14 (Fig. 2b). The brightness temperature at channel 14 (Fig. 2b) is the lowest in regions with overshooting (Fig. 2c) and the second lowest when there are opaque ice or overlapping clouds (Fig. 2c). Fog, water clouds, and cirrus are more difficult to see in a single channel, such as AHI
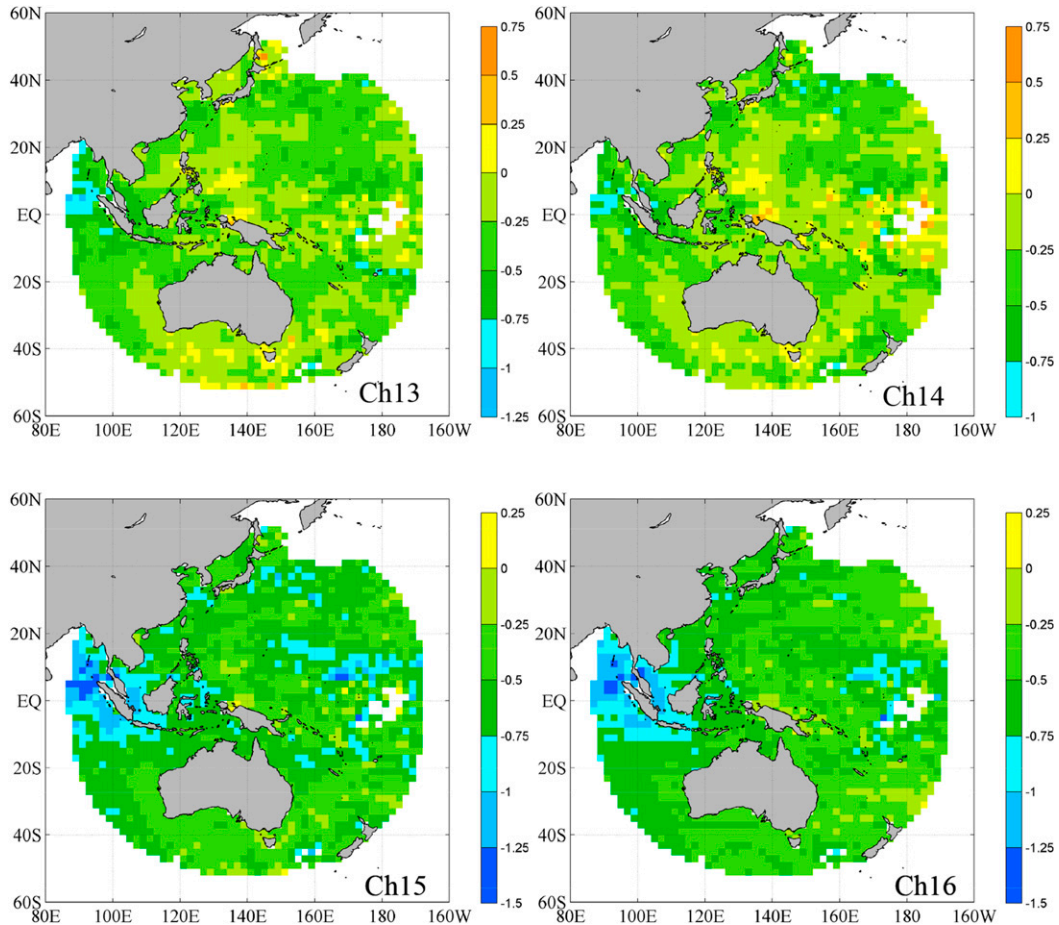
FIG. 5. (*Continued*)

visible channel 3 (Fig. 2a) or infrared channel 14 (Fig. 2b), than opaque ice or overlapping clouds. The probably cloudy pixels are located at the edges of cloudy regions (Fig. 2d). Almost no probably clear pixels are found in this case. The clear pixels in the cyan regions in Fig. 2d are finally selected for deriving AHI data biases and standard deviations separately over ocean and land.

Weather systems populated with clouds are often located in the same region in a short period, within a day or two. To minimize the data-void regions with clear AHI pixels over the full disk of AHI, the AHI data in the following 12 days in four different seasons are put together for the bias estimation of this study: 22–24 September and 15–17 December 2015, as well as 20–22 March and 5–7 June 2016. Figure 3a presents a composite map of areas that had clear pixels at least once (cyan) or no clear pixels (green) during the selected 12-day periods. The total data counts of clear-sky pixels within 2° × 2° grid boxes during the selected 12 days are provided in Fig. 3b. Most regions are observed with more than 100 clear AHI pixels in each 2° × 2° grid box except for some

regions in the tropics populated with clouds in the selected data period.

The initial AHI simulations using CRTM were found problematic when compared with those of RTTOV. For examples, the bias of AHI channel 16 estimated by the mean differences between AHI observations and CRTM simulations (i.e., $O - B^{CRTM}$) is as large as -1.20 K, while that estimated by the mean differences between AHI observations and RTTOV simulations (i.e., $O - B^{RTTOV}$) is only -0.35 K. Through a careful check of all input variables and parameters for the CRTM simulations, it was found that the AHI SRFs were updated in September 2013 at the JMA website,[2] but these updated SRFs were not implemented in CRTM. The differences between the updated and previous SRFs had caused bias differences in several channels of different magnitudes. Figure 4 shows the SRFs and the center frequencies of

---

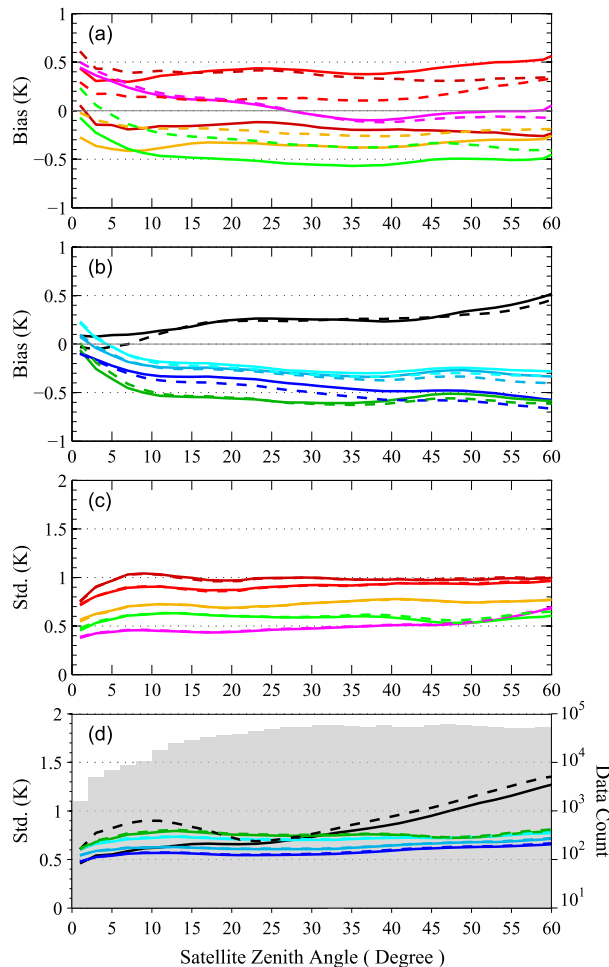[2] http://www.data.jma.go.jp/mscweb/en/himawari89/space_segment/spsg_ahi.html.

FIG. 6. Variations of (a),(b) biases and (c),(d) standard deviations of O − B$^{\mathrm{CRTM}}$ (solid) and O − B$^{\mathrm{RTTOV}}$ (dashed) differences with respect to satellite zenith angle at 2° intervals for AHI data for channels 7–16 over ocean. Data counts at 2° intervals are indicated in gray shading in (d). Color convention for different channels is the same as in Fig. 1.

FIG. 7. Variations of (a),(b) biases and (c),(d) data counts of O-B$^{\mathrm{CRTM}}$ (solid) and O-B$^{\mathrm{RTTOV}}$ (dashed) differences with respect to the scene brightness temperature at 1-K intervals for AHI data for channels 7–16 over ocean. Color convention for different channels is the same as in Fig. 1.

AHI channel 16 with and without using the updated SRFs. The center frequency of channel 16 shifted from a larger value (753.37 cm^{-1}) to a smaller value (754.13 cm^{-1}). Because the spectral radiances in channel 16 have strong slope, the SRF shift can cause a large difference between CRTM and RTTOV. In fact, the bias of AHI channel 16 calculated by O − B$^{\mathrm{CRTM}}$ with the updated AHI SRFs reduces to −0.52 K, which is comparable to that of RTTOV. In other words, a 0.24 cm^{-1} center frequency and SRF shift doubled the bias magnitude of channel 16.

b. AHI data biases and standard deviations over ocean

Bias characteristics of AHI infrared channels 7–16 over ocean are examined in terms of their spatial
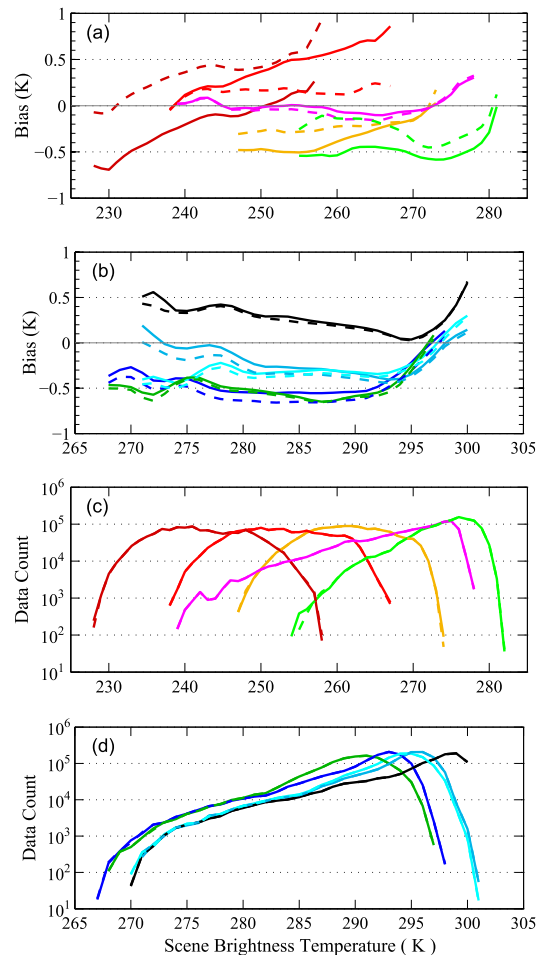
distributions, satellite zenith angle dependence, and scene temperature dependence.

The spatial distributions of biases of AHI channels 7–16 over ocean (Fig. 5) are calculated within 2° × 2° grid boxes and by using CRTM simulations with the updated SRFs. The AHI channel 7 (center wavenumber around 2575.94 cm^{-1}) has large positive biases in the middle latitudes in the Southern Hemisphere and the tropical central Pacific area. Small negative biases are found elsewhere. The AHI channel 9 has positive biases almost everywhere, implying that the model water vapor in the middle troposphere is probably systematically too wet. The stratospheric ozone channel 12 has small biases everywhere except for the tropical central Pacific area. Large positive biases in the tropical central Pacific, where the tropopause is usually high, could be associated with an inconsistent tropopause altitude between the model and reality. All other channels—that is,

TABLE 3. Bias (μ) and standard deviation (σ) between AHI observations and model simulations of brightness temperatures using either CRTMv2.2.3 or RTTOVv11.2 with the ECMWF analyses under clear-sky conditions for data with satellite zenith angles less than 60°. The surface emissivity model in RTTOVv11.2 is used in the CRTM simulations.

	Ocean				Land			
	μ (K)		σ (K)		μ (K)		σ (K)	
Channel No.	CRTM	RTTOV	CRTM	RTTOV	CRTM	RTTOV	CRTM	RTTOV
7	0.28	0.26	0.97	1.04	1.16	1.17	3.59	3.60
8	−0.17	0.37	1.09	1.09	−0.24	0.25	1.08	1.09
9	0.44	0.17	1.02	1.02	0.36	0.04	1.06	1.08
10	−0.34	−0.22	0.79	0.79	−0.37	−0.28	0.90	0.90
11	−0.45	−0.53	0.61	0.62	0.39	0.36	2.63	2.62
12	−0.01	−0.03	0.52	0.53	0.60	0.61	1.75	1.75
13	−0.30	−0.33	0.66	0.67	1.15	1.17	2.98	2.98
14	−0.26	−0.30	0.74	0.75	1.19	1.19	2.97	2.97
15	−0.56	−0.58	0.77	0.78	0.75	0.73	2.62	2.61
16	−0.52	−0.35	0.60	0.62	0.04	0.27	1.47	1.51

channels 8, 10, 11, 13–16—are characterized by negative biases in the full disk of AHI.

Variations of biases and standard deviations of $O − B^{CRTM}$ and $O − B^{RTTOV}$ differences with respect to the satellite zenith angle are shown in Fig. 6. Data counts at 2° interval are also provided in Fig. 6. The AHI biases and standard deviations do not have a significant dependence on the satellite zenith angle when satellite zenith angles are greater than 10° except for channel 7. The bias and standard deviation of $O − B$ differences of AHI channel 7 distinctly increase when the satellite zenith angle is greater than 45°. It could be a result of solar reflectance by sea ice during daytime. Since the solar reflectance by sea ice is not simulated in either CRTM or RTTOV, a larger $O − B$ difference could be caused by AHI channel 7. When satellite zenith angles are less than about 10°, most of channel biases decrease with satellite zenith angle except for channel 7. The satellite zenith angle dependence is possibly caused by the forward models. As pointed out by Chen et al. (2013), an excessive correction of sun-glint effect could bring a negative bias, which explains the bias dependence of channel 7 at low satellite zenith angle. Large differences between CRTM and RTTOV simulations are found for biases of channels 8–10 and 16 only (Fig. 6a). Since these are the channels with WFs located in the troposphere, it is possible that these differences come from the coefficients included in the two forward models. The coefficients in RTTOV were trained on the kCompressed Radiative Transfer Algorithm (kCARTA), while those in CRTM were trained on the Line-By-Line Radiative Transfer Model (LBLRTM; Saunders et al. 2007). The differences of the coefficients affect the simulated transmittances and thus brightness temperatures. Saunders et al.

(2007) conducted an intercomparison of 14 line-by-line and fast radiative transfer models. They pointed out that the transmittances computed by 14 models differ, particularly in the carbon dioxide channels (e.g., 14.966 μm). Also, RTTOV transmittances depart from the references more than the other models for the water vapor channels (e.g., 6.344 μm).

Variations of biases and data counts with respect to the scene brightness temperature at 1-K interval over ocean are examined in Fig. 7. All infrared channels seem to have scene-dependent biases, especially at high brightness temperatures. The strongest scene
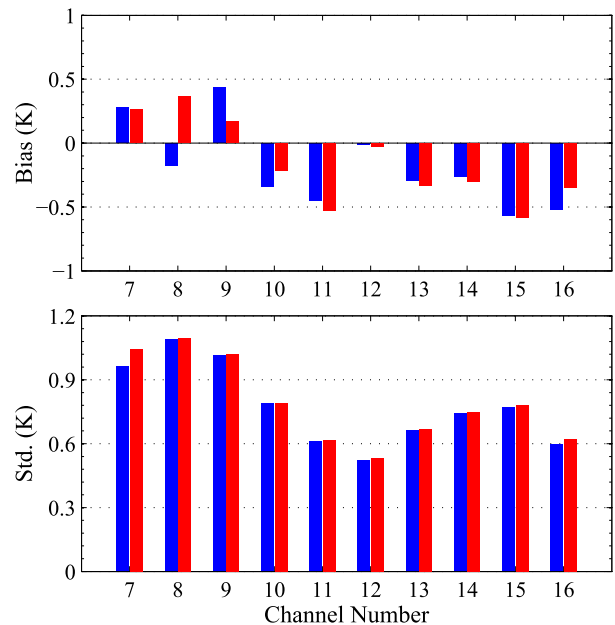

FIG. 8. (top) Biases and (bottom) standard deviations calculated by $O − B^{CRTM}$ (blue) and $O − B^{RTTOV}$ (red) statistics for all data over ocean with satellite zenith angles less than 60°.
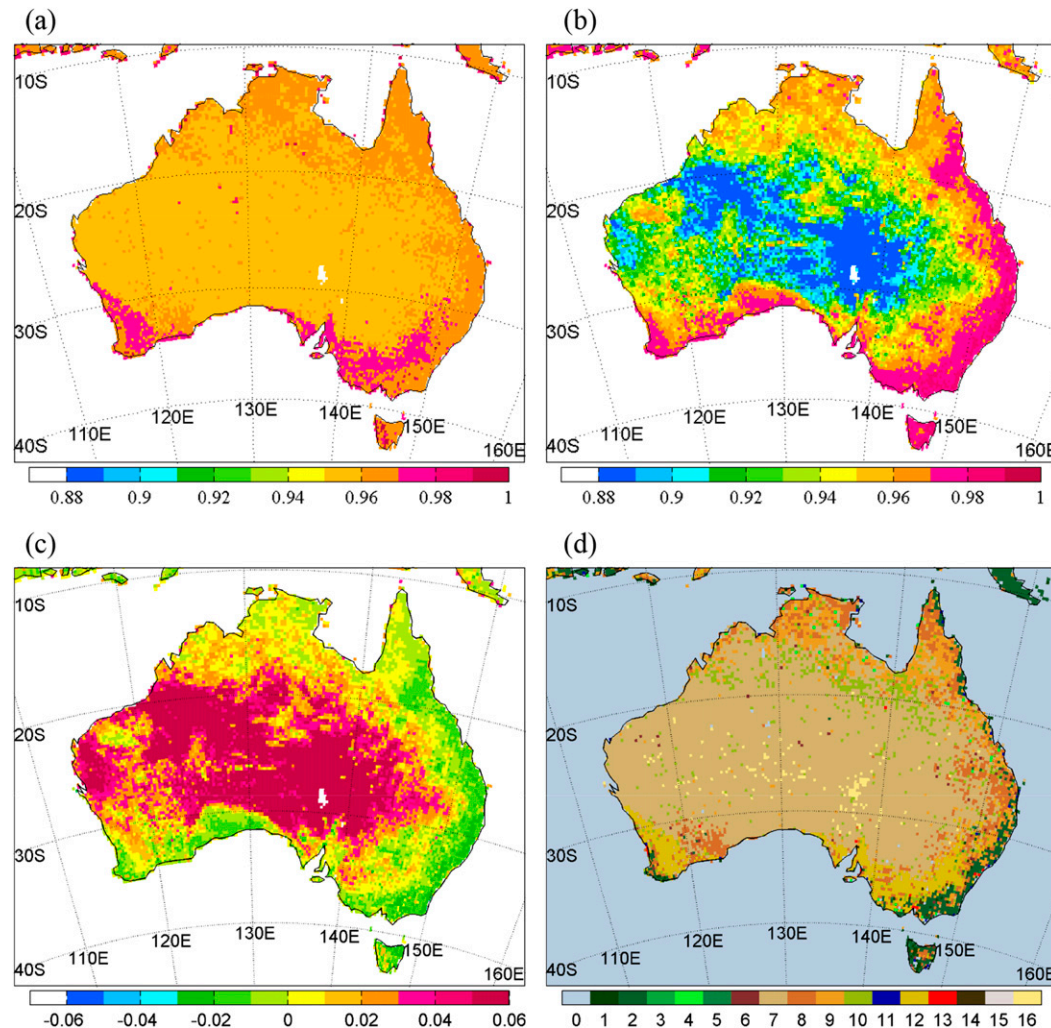
FIG. 9. Surface emissivity used in (a) CRTM at all times and (b) RTTOV in September. (c) Differences of surface emissivity for AHI channel 11 between CRTM and RTTOV over Australia. (d) Spatial distribution of the 17 surface types over Australia in the IGBP land-type scheme that are inputted into CRTM: water (0), evergreen needleleaf forest (1), evergreen broadleaf forest (2), deciduous needleleaf forest (3), deciduous broadleaf forest (4), mixed forest (5), closed shrubland (6), open shrubland (7), woody savannas (8), savannas (9), grassland (10), permanent wetlands (11), cropland (12), urban and built (13), cropland/natural vegetation mosaic (14), snow and ice (15), and barren or sparsely vegetated (16).

dependence of bias is found in channel 8. As indicated by Saunders et al. (2013), such strong scene-dependent biases are mainly caused by the instrument nonlinearity. Nearly all the infrared imagers, including AHI, are self-calibrated by using a blackbody inside the instrument as the heat target and the space as the cold target. The imagers are assumed to have a linear response with the incident radiation, ignoring mall nonlinearities that are present in reality. Note that the scene dependences of $O - B^{RTTOV}$ biases are not as significant as those of $O - B^{CRTM}$ biases for AHI water vapor channels 9 and 10. The difference of the coefficients between the two forward

models could be another possible cause of the scene-dependent biases. Differences of the variations of standard deviations between CRTM and RTTOV with respect to the scene brightness temperature observations are negligible (figures are omitted).

The spatially averaged biases and standard deviations calculated by CRTM and RTTOV for all data over ocean with satellite zenith angles less than 60° are provided in Table 3 and Fig. 8. The differences of biases of window channels 13–15 between CRTM and RTTOV are rather small, which indicates that the infrared sea surface emissivity model employed by CRTM (Wu and Smith 1997; Nalli et al. 2008) and RTTOV (Sherlock and
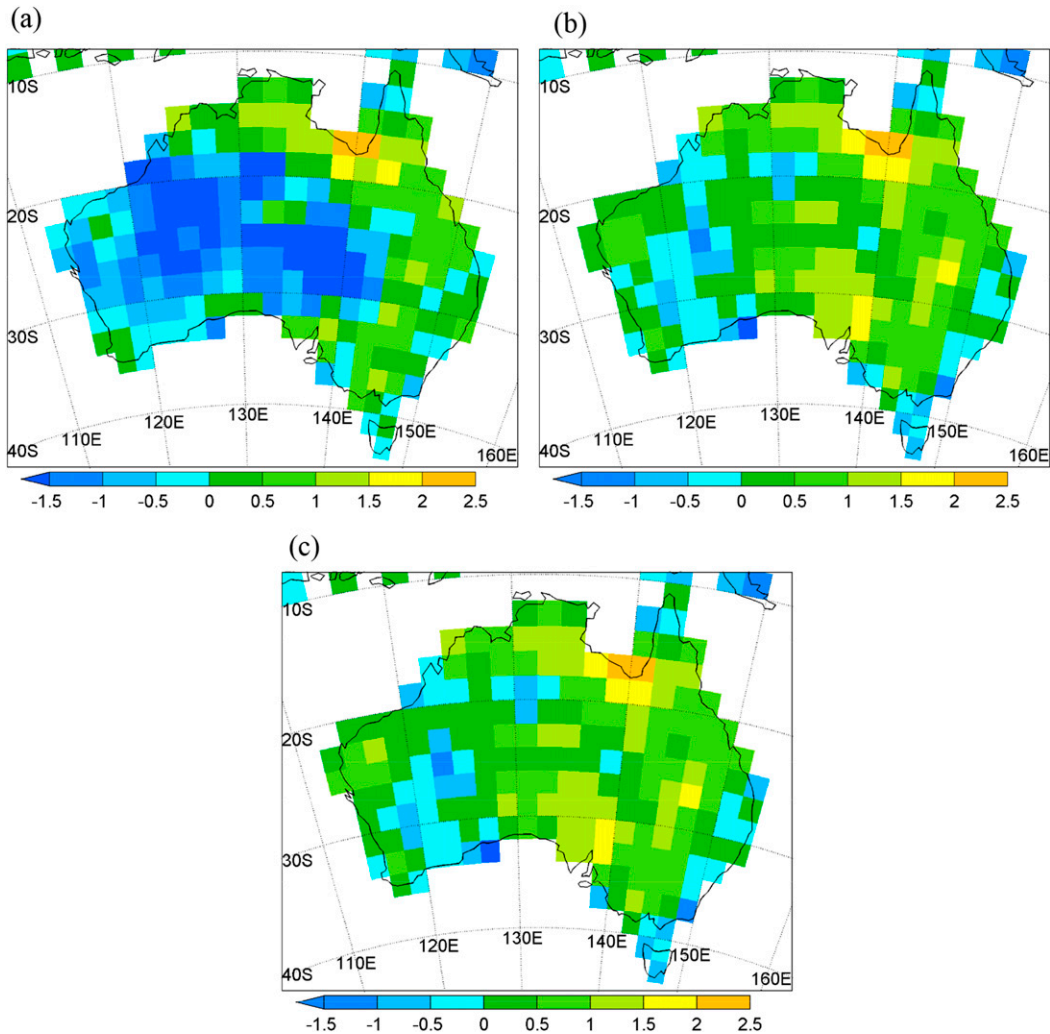
FIG. 10. Spatial distribution of O − B biases of AHI channel 11 within 2° × 2° grid boxes over Australia calculated using (a) CRTM and (b) RTTOV. (c) As in (a), but for replacing the surface emissivity model in CRTM with that in RTTOV.

Saunders 1999) are reasonably good and consistent. Differences of the O − B standard deviations between the two radiative transfer models are small over ocean.

c. AHI data biases and standard deviations over land

Over land, surface emissivity lookup tables (LUTs) are used in both CRTM and RTTOV. In CRTM, the LUT generates the emissivity as a function of wavenumber and surface type, whereas in RTTOV it is a function of wavenumber, latitude, longitude, and month (Vogel et al. 2011). The surface emissivity atlas in RTTOV is extracted from the University of Wisconsin Global Infrared Land Surface Emissivity (UWIREMIS) database (Seemann et al. 2008). Figure 9 shows the surface emissivity used in CRTM at all times (Fig. 9a) and RTTOV in September (Fig. 9b), and the differences

of surface emissivity between CRTM and RTTOV (Fig. 9c) for AHI channel 11 over Australia, as well as a spatial distribution of surface types around Australia. It is seen that differences of surface emissivity between CRTM and RTTOV near coastal areas are less than 0.03 except for the northwest coasts. However, large differences of more than 0.03–0.06 in surface emissivity between CRTM and RTTOV are found in mainland Australia, where the surface type is mostly open shrubland surface type. Such large differences in surface emissivity would make the CRTM-simulated brightness temperatures larger than those by RTTOV, resulting in the O − B^{CRTM} biases being much smaller than O − B^{RTTOV} over Australia. This is confirmed in Fig. 10, in which a spatial distribution of O − B biases of AHI channel 11 within 2° × 2° grid boxes over Australia
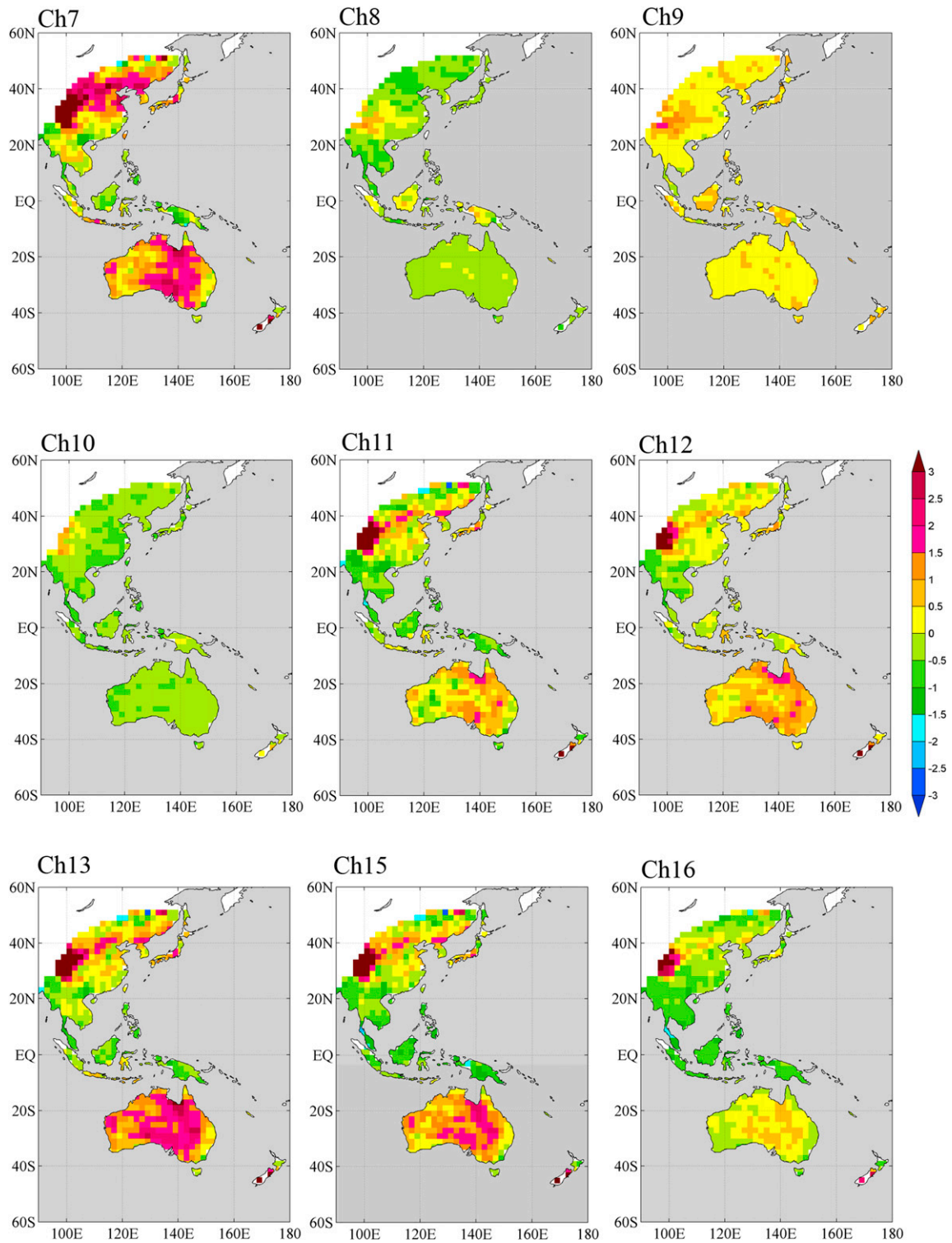
FIG. 11. Spatial distributions of $O - B^{CRTM}$ biases of AHI channels 7–13, 15, and 16 over land within $2° \times 2°$ grid boxes estimated by using CRTM with the RTTOV surface emissivity model. The bias distributions and magnitudes of channel 14 are similar to those of channel 13.
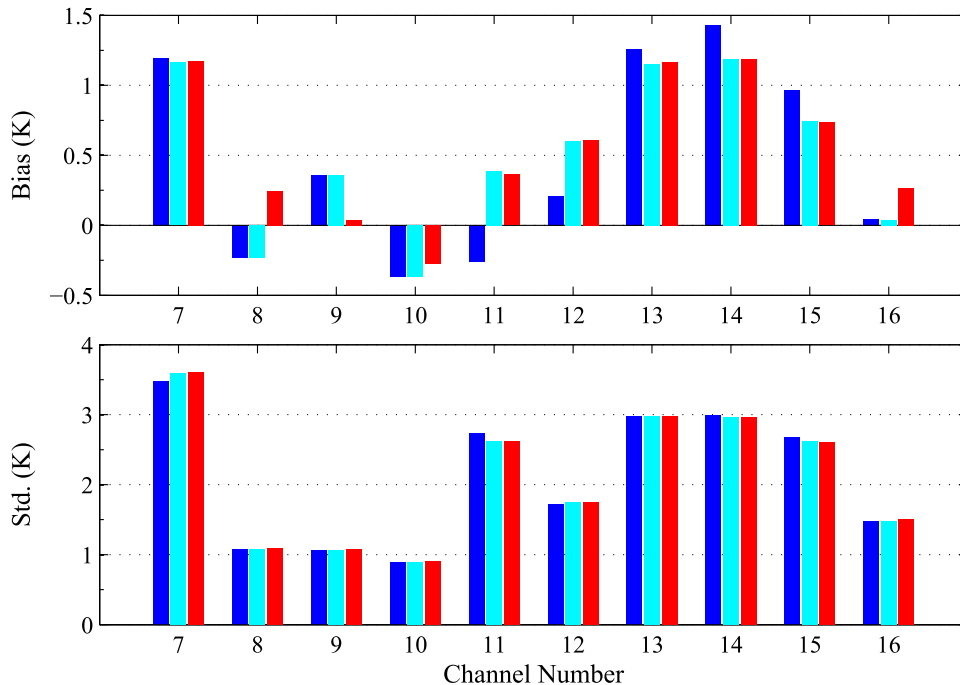
FIG. 12. (top) Biases and (bottom) standard deviations calculated by $O - B^{CRTM}$ (blue), $O - B^{CRTM}$ with surface emissivity model used in RTTOV v11.2 (cyan), and $O - B^{RTTOV}$ (red) over land.

calculated using CRTM and RTTOV is provided in Figs. 10a and 10b, respectively. If the surface emissivity model in CRTM is replaced with that of RTTOV, the bias distribution (Fig. 10c) resembles that of RTTOV (Fig. 10b).

Spatial distributions of $O - B$ biases over land for AHI channels 7–13, 15, and 16 using CRTM with the RTTOV surface emissivity model are provided in Fig. 11. The bias distributions and magnitudes of channel 14 are similar to those of channel 13 (figure is omitted). The $O - B$ biases for three water vapor channels are between ± 1 K. In contrast, the $O - B$ biases for the AHI surface-sensitive channels over land can be as large as several degrees. The largest biases are found over the Tibet Plateau, which resulted from a significant cold bias of the land skin temperature in the ECMWF analyses that are inputted into CRTM and RTTOV (Zhuo et al. 2016). The ECMWF land skin temperatures are slightly overestimated during nighttime and seriously underestimated during daytime (Trigo et al. 2015). The biased skin temperatures could bring a diurnal variation of the biases for AHI surface-sensitive channels over land, which will be investigated in a future study.

The spatially averaged biases and standard deviations calculated by CRTM and RTTOV for all data over land are provided in Table 3 and Fig. 12. Except for three water vapor channels and channel 16, which are affected by the tropospheric water vapor and temperature profiles,

the differences in model simulations between CRTM and RTTOV mainly come from the surface emissivity model used in each model. The large differences of biases between CRTM and RTTOV for three tropospheric water vapor channels 8–10 and carbon dioxide channel 16 are not as much affected by the surface emissivity as those AHI surface-sensitive channels.

5. Summary and conclusions

AHI is the first imager on a geostationary orbit that has more than 16 channels of measurements in the visible, near-infrared, and infrared parts of the electromagnetic spectrum. The AHI provides researchers and weather forecasters with better data sources and retrieval products for observing the Eastern Hemisphere in near–real time.

In this study, bias characteristics of AHI brightness temperatures between observations and model simulations for the 10 AHI infrared channels 7–16 used in NWP are estimated and compared between two of the most commonly used radiative transfer models: CRTM and RTTOV. The AHI biases of the 10 infrared channels over ocean and land are less than 0.6 and 1.2 K, respectively. Differences between the two radiative transfer models are mostly caused by the surface emissivity model except for the biases of the upper-tropospheric water vapor channels 8 and 9 and the

low-tropospheric carbon dioxide channel 16. It is shown that AHI biases are independent of satellite zenith angle except for channel 7 over ocean. A scene dependence of the AHI data biases is found for three water vapor channels. For the other seven infrared channels, the AHI data biases remain constant until reaching high brightness temperatures. Given the fact that the same input variables are used for the two radiative transfer models, the results in this study suggest that radiative transfer models themselves may have biases and must be taken care of in satellite data assimilation for NWP.

The ABI that will be on board the next generation of U.S. geostationary satellites (GOES-R, -S, -T, and -U) has designs in optics and calibration similar to the AHI. GOES-R is scheduled to be launched in November 2016. The AHI data bias estimation conducted in this study is helpful for future applications of ABI data.

REFERENCES

Bessho, K., and Coauthors, 2016: An introduction to Himawari-8/9—Japan's new-generation geostationary meteorological satellites. *J. Meteor. Soc. Japan*, **94**, 151–183, doi:10.2151/jmsj.2016-009.

Chen, Y., Y. Han, P. van Delst, and F. Weng, 2013: Assessment of shortwave infrared sea surface reflection and nonlocal thermodynamic equilibrium effects in the Community Radiative Transfer Model using IASI data. *J. Atmos. Oceanic Technol.*, **30**, 2152–2160, doi:10.1175/JTECH-D-12-00267.1.

Clark, S., 2014: Upgraded Japanese weather satellite set for launch. [Available online at http://spaceflightnow.com/2014/10/06/upgraded-japanese-weather-satellite-set-for-launch/.]

Gravelle, C. M., J. R. Mecikalski, W. E. Line, K. M. Bedka, R. A. Petersen, J. M. Sieglaff, G. T. Stano, and S. J. Goodman, 2016: Demonstration of a GOES-R satellite convective toolkit to "bridge the gap" between severe weather watches and warnings: An example from the 20 May 2013 Moore, Oklahoma, tornado outbreak. *Bull. Amer. Meteor. Soc.*, **97**, 69–84, doi:10.1175/BAMS-D-14-00054.1.

Han, Y., F. Weng, Q. Liu, and P. van Delst, 2007: A fast radiative transfer model for SSMIS upper atmosphere sounding channels. *J. Geophys. Res.*, **112**, D11121, doi:10.1029/2006JD008208.

Heidinger, A. K., 2011: ABI cloud mask. Version 2.0, NOAA/NESDIS/Center for Satellite Applications and Research Algorithm Theoretical Basis Doc., 93 pp.

——, A. T. Evan, M. J. Foster, and A. Walther, 2012: A naïve Bayesian cloud-detection scheme derived from CALIPSO and applied within PATMOS-x. *J. Appl. Meteor. Climatol.*, **51**, 1129–1144, doi:10.1175/JAMC-D-11-02.1.

Köpken, C., G. Kelly, and J.-N. Thépaut, 2004: Assimilation of Meteosat radiance data within the 4D-Var system at ECMWF: Assimilation experiments and forecast impact. *Quart. J. Roy. Meteor. Soc.*, **130**, 2277–2292, doi:10.1256/qj.02.230.

Lu, F., 2013: Preparing a seamless transition towards FY-4. *Fourth Asia/Oceania Meteorological Satellite Users' Conf.*, Melbourne, VIC, Australia, Bureau of Meteorology. [Available online at http://www.virtuallab.bom.gov.au/files/3513/8187/8770/s2_1350_Toward_a_seamless_transition_of_FY-4V2.pdf.]

Matricardi, M., F. Chevallier, G. Kelly, and J.-N. Thepaut, 2004: An improved general fast radiative transfer model for the assimilation of radiance observations. *Quart. J. Roy. Meteor. Soc.*, **130**, 153–173, doi:10.1256/qj.02.181.

Mecikalski, J. R., and K. M. Bedka, 2006: Forecasting convective initiation by monitoring the evolution of moving cumulus daytime GOES imagery. *Mon. Wea. Rev.*, **134**, 49–78, doi:10.1175/MWR3062.1.

——, S. J. Paech, K. M. Bedka, and L. A. Litten, 2008: A statistical evaluation of GOES cloud-top properties for nowcasting convective initiation. *Mon. Wea. Rev.*, **136**, 4899–4914, doi:10.1175/2008MWR2352.1.

——, J. K. Williams, C. P. Jewett, D. Ahijevych, A. LeRoy, and J. R. Walker, 2015: Probabilistic 0–1-h convective initiation nowcasts that combine geostationary satellite observations and numerical weather prediction model data. *J. Appl. Meteor. Climatol.*, **54**, 1039–1059, doi:10.1175/JAMC-D-14-0129.1.

Nalli, N. R., P. J. Minnett, and P. van Delst, 2008: Emissivity and reflection model for calculating unpolarized isotropic water surface-leaving radiance in the infrared. I: Theoretical development and calculations. *Appl. Opt.*, **47**, 3701–3721, doi:10.1364/AO.47.003701.

Ouaknine, J., and Coauthors, 2013: MTG Flexible Combined Imager optical design and performances. *Earth Observing Systems XVIII*, J. J. Bulter, X. Xiong, and X. Gu, Eds., International Society for Optical Engineering (SPIE Proceedings, Vol. 8866), 88661A, doi:10.1117/12.2023078.

Qin, Z., X. Zou, and F. Weng, 2013: Evaluating added benefits of assimilating GOES imager radiance data in GSI for coastal QPFs. *Mon. Wea. Rev.*, **141**, 75–92, doi:10.1175/MWR-D-12-00079.1.

Saunders, R. W., M. Matricardi, and P. Brunel, 1999: An improved fast radiative transfer model for assimilation of satellite radiance observations. *Quart. J. Roy. Meteor. Soc.*, **125**, 1407–1425, doi:10.1002/qj.1999.49712555615.

——, and Coauthors, 2007: A comparison of radiative transfer models for simulating Atmospheric Infrared Sounder (AIRS) radiances. *J. Geophys. Res.*, **112**, D01S90, doi:10.1029/2006JD007088.

——, T. A. Blackmore, B. Candy, P. N. Francis, and T. J. Hewison, 2013: Monitoring satellite radiance biases using NWP models. *IEEE Trans. Geosci. Remote Sens.*, **51**, 1124–1138, doi:10.1109/TGRS.2012.2229283.

Schmit, T. J., M. M. Gunshor, W. P. Menzel, J. J. Gurka, J. Li, and A. S. Bachmeier, 2005: Introducing the next-generation Advanced Baseline Imager on GOES-R. *Bull. Amer. Meteor. Soc.*, **86**, 1079–1096, doi:10.1175/BAMS-86-8-1079.

——, P. Griffith, M. M. Gunshor, J. M. Daniels, S. J. Goodman, and W. J. Lebair, 2016: A closer look at the ABI on the GOES-R series. *Bull. Amer. Meteor. Soc.*, doi:10.1175/BAMS-D-15-00230.1, in press.

Seemann, S. W., E. E. Borbas, R. O. Knuteson, G. R. Stephenson, and H.-L. Huang, 2008: Development of a global infrared land surface emissivity database for application to clear sky sounding retrieval from multispectral satellite radiances measurements. *J. Appl. Meteor. Climatol.*, **47**, 108–123, doi:10.1175/2007JAMC1590.1.

Sherlock, V., and R. Saunders, 1999: ISEM-6: Infrared surface emissivity model for RTTOV-6. Rep. for the EUMETSAT NWP SAF, Met Office, 16 pp.

Stengel, M., P. Undén, M. Lindskog, P. Dahlgren, N. Gustafsson, and R. Bennartz, 2009: Assimilation of SEVIRI infrared radiances with HIRLAM 4D-Var. *Quart. J. Roy. Meteor. Soc.*, **135**, 2100–2109, doi:10.1002/qj.501.

Szyndel, M. D. E., J.-N. Thépaut, and G. Kelly, 2005: Evaluation of potential benefit of SEVIRI water vapour radiance data from Meteosat-8 into global numerical weather prediction analyses. *Atmos. Sci. Lett.*, **6**, 105–111, doi:10.1002/asl.98.

Trigo, I. F., S. Boussetta, P. Viterbo, G. Balsamo, A. Beljaars, and I. Sandu, 2015: Comparison of model land skin temperature with remotely sensed estimates and assessment of surface-atmosphere coupling. *J. Geophys. Res. Atmos.*, **120**, 12 096–12 111, doi:10.1002/2015JD023812.

Velden, C. S., 1996: Winds derived from geostationary satellite moisture channel observations: Applications and impact on numerical weather prediction. *Meteor. Atmos. Phys.*, **60**, 37–46, doi:10.1007/BF01029784.

——, C. M. Hayden, S. J. Nieman, W. P. Menzel, S. Wazong, and J. S. Goerss, 1997: Upper-tropospheric winds derived from geostationary satellite water vapor observations. *Bull. Amer. Meteor. Soc.*, **78**, 173–195, doi:10.1175/1520-0477(1997)078<0173:UTWDFG>2.0.CO;2.

——, T. L. Olander, and S. Wazong, 1998: The impact of multi-spectral *GOES-8* wind information on Atlantic tropical cyclone track forecasts in 1995. Part I: Dataset methodology, description, and case analysis. *Mon. Wea. Rev.*, **126**, 1202–1218, doi:10.1175/1520-0493(1998)126<1202:TIOMGW>2.0.CO;2.

Vogel, R. L., Q. Liu, Y. Han, and F. Weng, 2011: Evaluating a satellite-derived global infrared land surface emissivity data set for use in radiative transfer modeling. *J. Geophys. Res.*, **116**, D08105, doi:10.1029/2010JD014679.

Weng, F., 2007: Advances in radiative transfer modeling in support of satellite data assimilation. *J. Atmos. Sci.*, **64**, 3799–3807, doi:10.1175/2007JAS2112.1.

Wu, X., and W. L. Smith, 1997: Emissivity of rough sea surface for 8–13 μm: Modeling and verification. *Appl. Opt.*, **36**, 2609–2619, doi:10.1364/AO.36.002609.

Yu, F., and X. Wu, 2016: Radiometric inter-calibration between Himawari-8 AHI and S-NPP VIIRS for the solar reflective bands. *Remote Sens.*, **8**, 165, doi:10.3390/rs8030165.

Zhuo, H., Y. Liu, and J. Jin, 2016: Improvement of land surface skin temperature simulation over the Tibetan Plateau and the associated impact on circulation in East Asia. *Atmos. Sci. Lett.*, **17**, 162–168, doi:10.1002/asl.638.

Zou, X., Z. Qin, and F. Weng, 2011: Improved coastal precipitation forecasts with direct assimilation of *GOES 11/12* imager radiances. *Mon. Wea. Rev.*, **139**, 3711–3729, doi:10.1175/MWR-D-10-05040.1.

——, ——, and Y. Zheng, 2015: Improved tropical storm forecasts with *GOES-13/15* imager radiance assimilation and asymmetric vortex initialization in HWRF. *Mon. Wea. Rev.*, **143**, 2485–2505, doi:10.1175/MWR-D-14-00223.1.